Management Systems in Production Engineering

2026, Volume 34, Issue 4, pp. 713-723

Date of submission of the article to the Editor: 05/2026
Date of acceptance of the article by the Editor: 10/2026

DOI 10.2478/mspe-2026-0058



LINKING SCAFFOLD ARCHITECTURE, ION TRANSPORT AND BIOFILM FORMATION IN FUNCTIONALIZED TPMS SCAFFOLDS USING A DIGITAL TWIN FRAMEWORK

Tatyana Ivakhniuk, Liudmyla Hrebenyk, Andrii Dyadyura
Sumy State University

Tibor Krenický
Technical University of Kosice

Liudmyla Primova, Irina Dyadyura
Sumy State University

Abstract:
Periprosthetic infections remain a major complication of orthopedic implants despite advances in antimicrobial surface functionalization. While antibacterial coatings can reduce bacterial colonization, local transport phenomena within porous implant architectures may generate spatially heterogeneous antimicrobial exposure, potentially influencing biofilm persistence. This study developed and experimentally validated a digital twin (DT) framework integrating scaffold morphology, computational fluid dynamics, antimicrobial ion transport, and bacterial colonization modelling to investigate the relationship between scaffold architecture and antibacterial performance. Triply periodic minimal surface (TPMS) hydroxyapatite scaffolds with gyroid and diamond architectures were fabricated and functionalized with an Ag–ZnO/HA nanocomposite coating. DT predictions were validated using micro-CT, SEM/EDS, ICP-OES, confocal laser scanning microscopy, microbiological assays, and quantitative PCR under dynamic perfusion bioreactor conditions. The gyroid architecture demonstrated superior antibacterial performance, achieving a 4.15 ± 0.41 log reduction in adherent bacteria compared with 3.42 ± 0.48 log for the diamond scaffold. CLSM revealed sparse, dispersed bacterial colonization in gyroid scaffolds, whereas diamond structures exhibited localized biofilm accumulation in regions associated with reduced transport. DT predictions showed good agreement with experimental observations (R^2 = 0.84). Bacteria recovered from low-transport regions of diamond scaffolds exhibited modest increases in Ag^+ MIC and activation of stress-response pathways, indicating adaptive physiological responses under heterogeneous antimicrobial exposure. Virtual optimization identified an improved gyroid configuration with a reduced unit cell size (350 µm). Experimental validation confirmed lower biofilm accumulation, more uniform Ag^+ distribution, and enhanced antibacterial performance without increasing antimicrobial loading. These findings demonstrate that scaffold topology influences antibacterial efficacy through its effect on local transport conditions and highlight the potential of digital twin methodologies as a supportive tool for the design and evaluation of antibacterial bone scaffolds.

Key words: digital twin, TPMS scaffold, Ion transport, biofilm formation, antibacterial performance, hydroxyapatite, Ag-ZnO nanocomposite

INTRODUCTION

Triply periodic minimal surface (TPMS) scaffolds have emerged as a promising class of porous biomaterials for bone tissue engineering because of their interconnected architecture, high surface-to-volume ratio, and controllable permeability. Unlike conventional strut-based lattices or stochastic porous

© 2026 Author(s). This is an open access article licensed under the Creative Commons BY 4.0 (https://creativecommons.org/licenses/by/4.0/)

structures, TPMS geometries are mathematically defined surfaces characterized by continuous curvature and periodicity in three dimensions [1, 2]. These features enable the fabrication of scaffolds with mechanical and transport properties that can be tailored to approximate those of trabecular bone [3, 4]. Previous studies have demonstrated that TPMS-based scaffolds exhibit favorable mechanical performance, reduced stress concentrations, and enhanced permeability compared with traditional lattice architectures [5, 6]. Their continuous pore network facilitates nutrient transport, cell migration, and osteoblast attachment, while the large available surface area supports tissue ingrowth and bone regeneration. As a result, TPMS structures have attracted considerable attention as candidate architectures for patient-specific bone implants manufactured using additive technologies. In parallel with advances in scaffold design, significant efforts have been devoted to the development of antibacterial biomaterials intended to reduce the risk of implant-associated infections. Despite the growing number of studies devoted to antibacterial TPMS scaffolds, the interaction between scaffold architecture, local fluid transport, and antimicrobial agent distribution remains insufficiently understood. Most experimental evaluations are based on static antibacterial assays that do not capture the spatial heterogeneity of ion transport and bacterial colonization within complex three-dimensional porous networks. Under dynamic conditions, regions characterized by low wall shear stress and limited convective transport may develop local sub-minimum inhibitory concentration (sub-MIC) gradients, creating favorable conditions for bacterial persistence and adaptive resistance responses [8]. To address this challenge, the present study proposes a digital twin (DT) framework integrating micro-CT-based geometry reconstruction, computational fluid dynamics (CFD), ion transport modelling, and agent-based microbial simulations. The study focuses on gyroid and diamond TPMS scaffolds functionalized with Ag-ZnO/HA nanocomposites. The objectives are: (i) to develop and experimentally validate the DT framework; (ii) to quantify the relationship between scaffold architecture, wall shear stress, local ion concentration, and biofilm formation; and (iii) to evaluate the potential of DT-assisted optimization for reducing bacterial colonization and improving antibacterial performance.

LITERATURE REVIEW

The development of infection-resistant bone scaffolds requires the integration of three complementary research areas: advanced scaffold architectures, antibacterial material functionalization, and predictive computational modelling. Recent studies have demonstrated significant progress in each of these domains; however, their combined application for predicting bacterial colonization within complex porous biomaterials remains limited. This section reviews current advances in TPMS-based scaffolds, antimicrobial nanocomposites, biofilm modelling, and digital twin technologies, with the aim of identifying the research gap addressed in the present work [9, 10, 11]. A key factor governing scaffold performance is the relationship between architecture and mass transport. In recent years, particular attention has been devoted to TPMS structures because of their ability to provide highly interconnected pore networks with controllable permeability and mechanical properties. Karaman et al. (2025) [12] performed a comprehensive computational investigation of fluid transport in Schwarz Primitive, Gyroid, and Diamond TPMS architectures, comparing network-solid and sheet-solid configurations. Using CFD, the authors evaluated permeability, pore size distribution, wall shear stress (WSS), flow velocity, and surface area, all of which are known to influence cell behaviour and tissue regeneration processes.

Despite these advances, the influence of TPMS geometry on the transport and spatial distribution of antibacterial agents remains insufficiently understood. The object of this research is TPMS-based architectures for patient-specific additively manufactured implants, including their topological design, transport characteristics, and biological performance. Within this context, understanding the early stages of biofilm formation requires consideration of the coupled interactions among bacterial cells, fluid flow, and scaffold geometry. Several computational approaches have been proposed to investigate microbial colonization under flow conditions. Lohrmann and Holm (2023) [13, 14] developed an agent-based modelling framework capable of simulating planktonic bacterial motion, surface attachment, and

biofilm development within a lattice-Boltzmann fluid environment [15]. Their results demonstrated that the interaction between fluid flow and bacterial motility plays a decisive role in determining attachment locations and subsequent colony morphology. The study also showed that biofilm mechanical properties and external hydrodynamic conditions significantly influence permeability and structural development. The influence of biofilm physical properties on flow behaviour in porous media has also been investigated extensively [16]. Numerical studies [17] have shown that decreasing biofilm permeability leads to increased boundary shear stress along preferential flow paths and alters the effective geometry of the porous network. Such feedback mechanisms demonstrate the importance of considering hydrodynamics and microbial growth as coupled processes rather than independent phenomena. Despite substantial progress in both TPMS scaffold design and biofilm modelling, an important knowledge gap remains [18–20]. Digital twin (DT) technology has recently emerged as a promising paradigm for predictive modelling in healthcare and biomedical engineering [21]. In infectious disease management, DTs have been proposed as tools for simulating pharmacokinetic and pharmacodynamic processes, optimizing antimicrobial therapy, supporting therapeutic drug monitoring, and improving clinical decision-making. Additional applications include modelling host–pathogen interactions, predicting disease progression, and supporting early diagnosis of severe infections. At a broader level, digital twins have been proposed for personalized medicine, immune system modelling, and hospital-scale process optimization [22, 23]. Within the field of biomaterials, digital twins are increasingly being explored for data-driven design, performance prediction, and optimization of implantable devices, including orthopedic implants and tissue-engineering scaffolds [4, 15]. Nevertheless, the application of digital twin technology to predict the spatial heterogeneity of antibacterial performance within TPMS-based scaffolds remains largely unexplored. In particular, no integrated framework has been reported that combines scaffold geometry, fluid dynamics, ion transport, and agent-based microbial behaviour to identify regions susceptible to sub-minimum inhibitory concentration (sub-MIC) exposure. Such regions are of particular interest because prolonged exposure to sub-MIC concentrations may promote bacterial persistence and adaptive stress response mechanisms even when the overall antibacterial performance of the material appears satisfactory. Based on these observations, the working hypothesis of the present study is that low-shear regions within TPMS scaffolds may generate local sub-MIC ion gradients that facilitate bacterial survival and adaptive responses. A digital twin framework integrating TPMS morphology, fluid transport, antimicrobial ion distribution, and microbial dynamics provides a suitable platform for investigating this hypothesis and for guiding the rational design of antibacterial scaffold architectures.

MATERIALS AND METHODS

Synthesis and Functionalization of Scaffolds

This study employs a multi-stage, interdisciplinary methodology that integrates computational design, additive manufacturing, and experimental characterisation to evaluate TPMS-based implant architectures. Calcium-deficient hydroxyapatite (CDHA) is synthesized in a continuous-mode chemical reactor using high-purity starting materials. Precursors are aqueous solutions of $(NH_4)_2HPO_4$, $Ca(NO_3)_2$, and $(NH_4)_2CO_3$. The reaction medium is adjusted to pH = 10.5 by adding 25% NH_4OH solution. The mixture is heated to 80°C for 10 minutes and then aged for 24 hours to allow complete precipitation and initial crystallization. Silver nanoparticles (Ag NPs, 20 nm, 99.9%, Sigma-Aldrich) and zinc oxide nanoparticles (ZnO NPs, 40 nm, 99.8%, NanoAmor) were used as received. Scaffold digital models were designed using nTopology 4.0 (nTopology Inc., NY, USA) with gyroid (G) and diamond (D) TPMS unit cells defined by the implicit equations:

- Gyroid:
  $\sin(x)\cos(y) + \sin(y)\cos(z) + \sin(z)\cos(x) = c$, where $c = 0$ (for minimal surface, porosity ~75%).
- Diamond:
  $\sin(x)\sin(y)\sin(z) + \sin(x)\cos(y)\cos(z) + \cos(x)\sin(y)\cos(z) + \cos(x)\cos(y)\sin(z) = c$

Unit cell size was set to 500 µm (baseline) and 350 µm (optimized). Wall thickness was fixed at 150 µm. Scaffold dimensions: cylindrical, Ø = 6 mm, height = 4 mm. The STL files were exported to a stereolithography printer (Nanoscribe Photonic Professional GT2, Germany) equipped with a 25 µm resolution objective.

Morphological and Physicochemical Characterization. Scaffolds were scanned using a SkyScan 1276 (Bruker, Kontich, Belgium) at 50 kV, 200 µA, with an aluminum filter (0.5 mm). Pore size distribution and strut thickness were analyzed using CTAn (Bruker) with the local thickness algorithm. Surface meshes were generated using Avizo 2023 (Thermo Fisher) with an adaptive thresholding and marching cubes algorithm, then exported as STL and PLY formats for DT construction.

Scanning Electron Microscopy (SEM) and Energy Dispersive X-ray Spectroscopy (EDS). Scaffold morphology and nanocomposite distribution were examined using a JEOL JSM-7800F field emission SEM at 5 kV acceleration voltage. Samples were sputter-coated with 5 nm of iridium. EDS mapping (Oxford X-Max 80 mm²) was performed at 15 kV to quantify Ag and Zn distribution on the scaffold surface and across cross-sections (embedded in epoxy resin and polished).

Ag^+/Zn^{2+} Release Kinetics (Static Conditions). Pre-weighed scaffolds (n = 3 per composition) were immersed in 10 mL phosphate-buffered saline (PBS, pH 7.4, 37°C) in sealed polypropylene tubes. At predetermined time points (1, 3, 6, 12, 24, 48, 72, 120, 168 h), 1 mL of supernatant was withdrawn and replaced with fresh PBS. Ag^+ and Zn^{2+} concentrations were measured using inductively coupled plasma optical emission spectrometry (ICP-OES, PerkinElmer Optima 8300) at wavelengths 328.068 nm (Ag) and 213.857 nm (Zn). Detection limits were 0.5 ppb (Ag) and 0.2 ppb (Zn).

Geometry Layer (Morphological Domain). Micro-CT derived surface meshes were converted to watertight NURBS models using Rhinoceros 7 with the Griddle plugin. The models were then imported into OpenFOAM v11 for meshing. A conformal hexahedral mesh was generated using snappyHexMesh with three levels of refinement near solid walls (final cell size 5 µm near walls, 20 µm in the bulk). Mesh quality was verified: non-orthogonality < 70°, skewness < 4, aspect ratio < 10. The final mesh contained 2.4 ± 0.3 million cells per unit cell.

Agent definition: two bacterial species were modeled: *Staphylococcus aureus* (ATCC 25923, spherical, diameter 1 µm) and *Escherichia coli* (ATCC 25922, rod-shaped, length 2 µm, width 0.8 µm). Agents were initialized as 1,000 planktonic cells of each species uniformly distributed at the inlet face at t = 0. Each agent maintained a state vector: {position, species, state (planktonic/reversibly attached/irreversibly attached/EPS-producing/dead), age, division timer, stress level (primed for resistance), efflux pump activity (0-1)}. Adhesion kinetics: The probability of a planktonic cell transitioning to reversible adhesion within a time step Δt was:

$$P_{adh} = 1 - \exp\left(-k_{adh} \cdot \Delta t \cdot \exp\left(-\frac{WSS}{WSS_0}\right)\right), \quad (1)$$

where:

k_{adh} = 0.05 s^{-1} (baseline adhesion rate),

WSS_0 = 0.02 Pa (shear stress at which adhesion probability halves).

Reversible adhesion became irreversible after 300 s (5 min) of uninterrupted contact.

Growth and division: The specific growth rate µ followed Monod kinetics with inhibition by Ag^+ and Zn^{2+}:

$$\mu = \mu_{max} \cdot \frac{N}{K_N+N} \cdot \frac{1}{1+(C_{Ag}/MIC_{Ag})^n} \cdot \frac{1}{1+(C_{Zn}/MIC_{Zn})^n}, \quad (2)$$

where:

μ_{max} = 0.033 min^{-1} (*S. aureus*) and 0.05 min^{-1} (*E. coli*);

N is local nutrient concentration (fixed);

K_N = 0.1 g/L; C_{Ag} and C_{Zn} are local ion concentrations;

MIC_{Ag} = 0.5 ppm (*S. aureus*) and 0.8 ppm (*E. coli*);

MIC_{Zn} = 2 ppm (both); n = 2 (Hill coefficient).

Division occurred when the division timer exceeded 1/µ.

Death: For [Ag^+] > MIC_Ag, death probability per time step was set to 0.95 (ensuring rapid clearance).

Simulation protocol: Each DT simulation ran for 72 h simulated time with Δt = 60 s, saving snapshots every 6 h. Three independent runs were performed per condition (scaffold type, cell size, flow rate). Output metrics included: biofilm-covered surface area (%), total viable cells per scaffold, spatial distribution of live/dead cells, and proportion of cells in "primed" state.

Experimental Validation.

Bacterial Strains and Culture Conditions. The study utilized reference strains of *S. aureus* ATCC 25923 and *E. coli* ATCC 25922. The authenticity of the test strains and their basic biological properties were confirmed by culture certificates.

Perfusion Bioreactor Setup. A custom-built perfusion bioreactor (Biorep Technologies, Miami, FL, USA) consisting of six parallel flow chambers was used.

Biofilm Quantification (Confocal Laser Scanning Microscopy). At each endpoint (24, 48, 72 h), scaffolds were carefully removed from the chambers, gently rinsed with PBS to remove non-adherent bacteria, and stained using the LIVE/DEAD BacLight Bacterial Viability Kit (L7012, Invitrogen).

Planktonic and Adherent CFU Enumeration. For each scaffold, the effluent medium was serially diluted in PBS and plated on tryptic soy agar (TSA) in duplicate. To differentiate *S. aureus* and *E. coli*, mannitol salt agar (MSA, selective for staphylococci) and MacConkey agar (selective for gram-negative rods) were used.

Flow Cytometry. To assess viability and membrane integrity of planktonic bacteria in the effluent, 500 µL samples were stained with SYTO9/PI (same concentrations as above) for 15 min at room temperature. Flow cytometry was performed on a BD FACSCanto II equipped with 488 nm (blue) and 561 nm (yellow-green) lasers. SYTO9 fluorescence was detected in the FITC channel (530/30 nm), PI in the PE-Texas Red channel (585/42 nm). A minimum of 50,000 events were acquired per sample. Data were analyzed using FlowJo 10.8. Live cells were defined as $SYTO9^+/PI^-$, dead as PI^+, and damaged as $SYTO9^+/PI^+$.

Ion Concentration Profiling (ICP-OES). After the 72 h experiment, scaffolds were sectioned into three concentric zones (core: $\varnothing < 2$ mm, mid: $2 < \varnothing < 4$ mm, shell: $\varnothing > 4$ mm) using a microtome (Leica RM2255). Each section was dissolved in 2 mL of 5% HNO_3 (trace metal grade, Fisher) at 60°C for 4 h. The solution was diluted to 5 mL with ultrapure water, filtered (0.22 µm), and analyzed by ICP-OES as described in section 3.2.3.

Ethidium Bromide Accumulation Assay (Efflux Activity). To quantify active bacterial efflux pump activity triggered by sub-MIC ion exposure, an ethidium bromide (EtBr) accumulation assay was performed on isolates recovered from different scaffold zones.

Gene Expression Analysis via Quantitative PCR (qPCR). Total RNA was extracted from *S. aureus* and *E. coli* cells recovered from the concentric core and shell layers of the scaffolds using the RNeasy Mini Kit (Qiagen, Germany). RNA concentration and purity were checked spectrophotometrically.

In Silico Optimization Using the Digital Twin.

Once the DT was validated against experimental data ($R^2 \geq 0.85$ for all major outputs), it was used to perform a virtual design space exploration. The following parameters were varied independently (Table 1).

Table 1

Input parameter space and design variables for the in silico optimization framework

Parameter	Range/Values	Step/Design
TPMS type	Gyroid, Diamond, Primitive	Categorical
Unit cell size	300 µm – 700 µm	50 µm increments
Wall thickness	100 µm – 200 µm	25 µm increments
Inlet flow velocity	0.05 – 0.5 mm/s (physiological range)	0.05 mm/s steps
Ag loading	2 wt% – 8 wt%	1 wt% steps

A total of 24 parameter combinations were simulated (full factorial for categorical factors, Latin hypercube sampling for continuous factors). Each simulation required approximately 8 h on the

GPU-accelerated workstation. The primary output for optimization was biofilm volume fraction (total volume occupied by live bacteria + EPS divided by scaffold pore volume) at 72 h. Secondary outputs included spatial heterogeneity index (coefficient of variation of biofilm thickness) and predicted emergence of primed cells (proportion > 0.1% was considered a red flag).

The optimal design was defined as the combination that minimized biofilm volume fraction while maintaining mechanical feasibility (wall thickness ≥ 100 µm, porosity ≤ 80%). This optimal design was then fabricated and experimentally tested in triplicate using the same protocols described above to validate the DT's predictive capability.

Statistical Analysis. All experiments were performed with at least n = 3 independent biological replicates (each replicate used a separately printed scaffold and fresh bacterial culture). Data are presented as mean ± standard deviation (SD). Normality was assessed by Shapiro-Wilk test; homogeneity of variances by Levene's test. Comparison between two groups: two-tailed Student's t-test (parametric) or Mann-Whitney U test (non-parametric). Multiple comparisons: one-way or two-way analysis of variance (ANOVA) followed by Tukey's HSD post-hoc test. Correlation between DT predictions and experimental measurements: Pearson's correlation coefficient (r) and coefficient of determination (R^2). Root mean square error (RMSE) and mean absolute percentage error (MAPE) were also computed.

Significance level: $\alpha = 0.05$ ($p < 0.05$ considered significant; $p < 0.01$ highly significant). Statistical analyses were performed using GraphPad Prism 10.0 and R 4.3.1.

RESULTS AND DISCUSSION

SEM imaging demonstrated successful deposition of the Ag-ZnO/HA nanocomposite on both TPMS architectures [24]. The coating covered the scaffold surfaces uniformly, although isolated nanoparticle agglomerates with dimensions below 2-3 µm were occasionally observed. EDS elemental mapping confirmed the presence of both Ag and Zn throughout the analyzed regions, with no evidence of large-scale elemental segregation. Quantitative analysis yielded Ag and Zn atomic ratios of 0.018 ± 0.003 and 0.022 ± 0.004, respectively. Minor local variations in elemental distribution were detected, which are expected for nanoparticle-based coatings and may contribute to local differences in ion release behavior. Fig. 1 presents representative micro-CT reconstructions and SEM observations of the fabricated scaffolds.

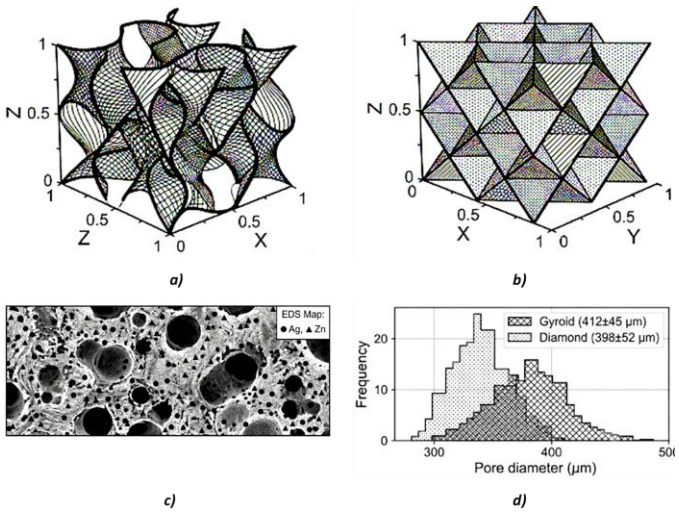


Fig. 1 Morphological characterization and pore size distribution of the fabricated TPMS scaffolds.
a) 3D micro-CT surface reconstruction of the gyroid scaffold architecture
b) 3D micro-CT surface reconstruction of the diamond scaffold architecture
c) Cross-sectional SEM micrograph with elemental EDS mapping overlay showcasing the uniform Ag-ZnO nanocomposite coating distribution
d) Unimodal pore diameter distribution analysis determined via micro-CT local thickness algorithms (data present mean ± SD, (n = 3).
Alt-text: *Four-panel comparison of gyroid and diamond TPMS geometries, Ag-Zn EDS coating distribution, and their overlapping pore-size distributions.*

Both architectures exhibited high geometric fidelity relative to the original CAD models. The measured porosity values differed by less than 4% from the design targets. Analysis of pore size distribution revealed a predominantly unimodal structure, with mean pore diameters of 412 ± 45 µm for the gyroid scaffold and 398 ± 52 µm for the diamond scaffold. While the overall pore characteristics were comparable, the diamond architecture contained a greater number of locally concave regions and geometrically confined passages, which may influence local transport phenomena under flow conditions.
CFD simulations revealed noticeable differences in flow behavior between the two TPMS architectures despite their similar global porosity. In both cases, the flow regime remained laminar (Re < 0.1), and fluid transport was dominated by the scaffold geometry. The gyroid architecture promoted relatively uniform velocity distributions and continuous flow pathways throughout the porous network. Fig. 2 summarizes the hydrodynamic analysis.

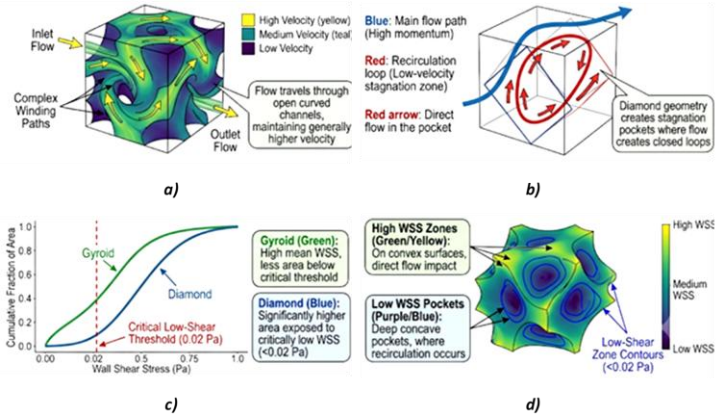


Fig. 2. Computational fluid dynamics (CFD) and wall shear stress (WSS) analysis within the porous networks.
a) Velocity streamlines in the gyroid cell indicating uniform continuous pathways
b) Flow feature characterization in the diamond cell highlighting recirculation pockets and fluid stagnation zones
c) Cumulative WSS distribution comparison emphasizing the critical low-shear area threshold (< 0.02 Pa)
d) Spatially resolved WSS distribution map on the diamond surface detailing high-momentum zones and low-shear pockets.
Alt-text: *Four-panel CFD view comparing gyroid and diamond flow, cumulative wall-shear-stress curves, and low-shear pockets in the diamond scaffold.*

The WSS distribution was heterogeneous for both architectures; however, the extent of low-shear regions differed substantially. The gyroid scaffold showed a narrower WSS distribution with fewer surface regions exposed to values below 0.02 Pa. The diamond architecture displayed a broader distribution and a greater proportion of low-shear areas.
The simulated transport of Ag^{+} and Zn^{2+} ions demonstrated that scaffold architecture affected not only fluid flow but also the spatial distribution of antimicrobial species. In both TPMS designs, ion concentrations gradually increased during the first 48 h and approached quasi-steady-state conditions thereafter. However, local concentration heterogeneity was observed throughout the scaffold volume.
The gyroid scaffold exhibited relatively uniform ion penetration across the porous network, whereas the diamond architecture developed regions with lower local concentrations in geometrically confined areas. These differences became more pronounced at intermediate time points (24-48 h), when convective transport and release kinetics interacted most strongly. These findings suggest that scaffold topology can influence antimicrobial performance indirectly through its effect on local transport processes. Even when the total amount of released ions remains similar, spatial heterogeneity may create microenvironments characterized by reduced antimicrobial exposure. Following 72 h of perfusion culture with a mixed inoculum of *S. aureus* and *E. coli* (10^7 CFU/mL each), extensive biofilm formation was observed on non-functionalized HA scaffolds irrespective of architecture. Total adherent bacterial counts reached

$(1.1 \pm 0.3) \times 10^9$ CFU and $(1.3 \pm 0.4) \times 10^9$ CFU for the gyroid and diamond controls, respectively, with no statistically significant difference between the two architectures ($p > 0.05$). LIVE/DEAD staining indicated high bacterial viability in both control groups (87 ± 5% and 91 ± 4%, respectively). Functionalization with the Ag-ZnO/HA nanocomposite substantially reduced bacterial colonization in both scaffold architectures (Table 2).

Table 2

Quantitative microbiological analysis and bacterial viability after 72 h of dynamic perfusion culture

Scaffold type	Total adherent CFU (72 h)	Log reduction vs control	Viability (%)
HA Gyroid	$(1.1 \pm 0.3)\times10^9$	–	87 ± 5
HA Diamond	$(1.3 \pm 0.4)\times10^9$	–	91 ± 4
Ag-ZnO/HA Gyroid	$(7.8 \pm 2.4)\times10^4$	4.15 ± 0.41	9.4 ± 2.3
Ag-ZnO/HA Diamond	$(4.9 \pm 1.7)\times10^5$	3.42 ± 0.48	18.7 ± 4.8

Note: data are presented as mean ± SD (n = 3). CFU: Colony Forming Units; HA: Hydroxyapatite.

The gyroid scaffold exhibited a residual bacterial burden of $(7.8 \pm 2.4) \times 10^4$ CFU, corresponding to a 4.15 ± 0.41 log reduction relative to the non-functionalized control. The diamond scaffold showed a higher residual bacterial load of $(4.9 \pm 1.7) \times 10^5$ CFU and a corresponding reduction of 3.42 ± 0.48 log. The difference between the two functionalized architectures was statistically significant ($p < 0.05$), indicating that scaffold geometry influenced antibacterial performance despite identical coating composition. The proportion of viable cells determined by CLSM decreased from approximately 90% in the control groups to 9.4 ± 2.3% and 18.7 ± 4.8% for the functionalized gyroid and diamond scaffolds, respectively (Table 2). Although both architectures demonstrated strong antibacterial activity, the gyroid scaffold consistently exhibited lower bacterial survival and reduced biofilm coverage. Confocal microscopy further revealed that residual bacterial populations were not uniformly distributed throughout the scaffold volume. In the gyroid architecture, surviving cells were predominantly detected as isolated cells or small microcolonies (<20 μm) dispersed across the scaffold surface. In contrast, the diamond architecture exhibited localized bacterial aggregates ranging from approximately 30 to 90 μm in diameter, preferentially associated with regions predicted by the DT to experience reduced local transport and lower antimicrobial exposure. Table 2 summarizes the quantitative microbiological results obtained after 72 h of perfusion culture. While both TPMS architectures benefited from Ag-ZnO/HA functionalization, the superior performance of the gyroid geometry suggests that scaffold topology influences the local availability of antimicrobial ions and consequently affects bacterial survival.

The DT predicted distinct spatial patterns of residual bacterial colonization in the two scaffold architectures. In the gyroid scaffold, surviving bacteria were predicted to occur predominantly as isolated cells or small microcolonies (<15 μm) distributed throughout the accessible pore network, without pronounced spatial clustering. In contrast, the diamond architecture was predicted to support localized biofilm accumulation within concave regions characterized by reduced wall shear stress and lower local antimicrobial ion concentrations. Overlay analysis demonstrated spatial correspondence between regions predicted to be susceptible to biofilm persistence and experimentally observed bacterial accumulation. The agreement between predicted and measured biofilm volume fractions yielded $R^2 = 0.84$ with an RMSE of 6.1%. To further examine the relationship between hydrodynamics, antimicrobial transport, and bacterial colonization, biofilm biomass was analyzed as a function of local wall shear stress and Ag^+ concentration. Regions exposed to WSS values below 0.02 Pa exhibited approximately 2.6-fold higher live biofilm biomass than regions with WSS exceeding 0.05 Pa. Similarly, scaffold regions where Ag^+ concentrations remained below 0.60 ppm showed a 2.1-fold increase in viable bacterial coverage relative to regions exposed to higher ion concentrations. The optimized architecture exhibited improved antibacterial performance, reduced biofilm accumulation, and more uniform antimicrobial ion distribution, demonstrating the utility of the DT framework for guiding scaffold design and experimental optimization (Table 3).

Table 3

Comparative evaluation of experimental and digital twin outcomes for baseline and optimized gyroid scaffold architectures

Parameter	Baseline Gyroid (500 μm)	Optimized Gyroid (350 μm)	p-value
Log reduction (vs. control)	4.15 ± 0.41	4.92 ± 0.32	< 0.05
Biofilm volume fraction (%)	12.4 ± 1.8 (exp), 13.1 (DT)	6.9 ± 1.5 (exp), 7.2 (DT)	< 0.01
Core Ag^+ concentration (ppm)	0.52 ± 0.06	0.64 ± 0.08	< 0.05
Cells with elevated efflux activity (%)	0.18 ± 0.06	0.07 ± 0.03	< 0.05
sigB fold change	2.1 ± 0.5	1.3 ± 0.3	< 0.05

Note: significant differences are indicated by p-values. DT: Digital Twin; WSS: Wall Shear Stress.

The present results demonstrate that scaffold architecture can influence antibacterial performance to a degree comparable with modifications in antimicrobial loading. Although both TPMS designs possessed similar porosity and surface area, differences in local transport conditions resulted in measurable variations in ion distribution, bacterial survival, and biofilm organization. These findings highlight the importance of considering mass transport phenomena during the design of antibacterial scaffolds. The digital twin provided a useful framework for integrating geometric, hydrodynamic, and microbiological information into a single predictive platform. While additional validation under more complex biological conditions is required, the approach may support the identification of scaffold configurations that warrant experimental investigation and reduce reliance on purely empirical design strategies.

CONCLUSIONS

This study developed and experimentally validated a digital twin framework integrating scaffold morphology, computational fluid dynamics, antimicrobial ion transport, and bacterial colonization modelling to investigate the influence of TPMS architecture on antibacterial performance. The results demonstrated that scaffold topology significantly affected local transport conditions despite comparable porosity and surface area. The gyroid architecture promoted more uniform flow and antimicrobial ion distribution, resulting in lower bacterial survival, reduced biofilm accumulation, and fewer regions exposed to reduced antimicrobial concentrations than the diamond scaffold.

Spatial predictions generated by the digital twin were consistent with experimental observations obtained by CLSM, ICP-OES, microbiological assays, and gene expression analysis. The model was able to identify architectural features associated with increased probability of bacterial persistence. Virtual design optimization suggested that reducing gyroid unit cell size from 500 μm to 350 μm improved transport uniformity and further reduced biofilm formation without increasing antimicrobial loading. Experimental testing of the optimized scaffold confirmed the principal trends predicted by the model. Overall, the findings highlight the importance of coupling scaffold architecture with transport-driven antimicrobial performance and demonstrate the potential of digital twin methodologies as a supportive tool for the rational design and evaluation of antibacterial bone scaffolds. Limitations of the present study include the use of a simplified dual-species bacterial model, the absence of host immune interactions, and the relatively short experimental observation period. Future work should incorporate more complex polymicrobial systems, host-response mechanisms, and long-term validation under physiologically relevant flow conditions.

ACKNOWLEDGMENTS

This work was funded by the Ministry of Education, Science, Research, and Sport of the Slovak Republic within projects VEGA 1/0834/25 and KEGA 012TUKE-4/2025.

REFERENCES

[1] Panda, A., Dyadyura, K.O., Ivakhniuk, T.V., Hrebenyk, L., Primova, L.O. (2024) Nano-materials in dental implants-understanding composition and biofilm dynamics. *MM Science Journal*, pp. 8050-8057.

[2] Safavi, S., Gray, H.A., Lee, P.V.S. (2025) Design and optimisation of patient-specific porous femoral stems. *J. Orthop. Surg. Res*. 20, 1002.

[3] Gallego, S.G., Cheu, L.E.R. (2026) 3D-printed hip prostheses with regenerative integration: a state-of-the-art comprehensive review. Front. *Bioeng. Biotechnol*. 13, 1719810.

[4] Gabrieli, R., Wenger, R., Mazza, M., Verné, E., Baino, F. Design, (2024) Stereolithographic 3D Printing, and Characterization of TPMS Scaffolds. *Materials*. 17, 654.

[5] Han, X., Yang, D., Yang, C., Spintzyk, S., Scheideler, L., Li, P., Li, D., Geis-Gerstorfer, J., Rupp, F. (2019) Carbon fiber reinforced PEEK composites based on 3D-printing technology for orthopedic and dental applications. *J. Clin. Med*. 8, 240.

[6] Sun, Y., Wang, Y., Ji, C., Li, Y., Ma, J. (2025) Design and performance study of biomimetic bone scaffolds based on the fusion of triply periodic minimal surfaces. *BMC Musculoskelet. Disord*. 27, 50.

[7] Ceddia, M., Solarino, G., Dramisino, P., De Giosa, G., Rizzo, S., Trentadue, B. (2024) Comparison of Stress between Three Different Functionally Graded Hip Stem Implants Made of Different Titanium Alloys and Composite Materials. *J. Compos. Sci*. 8, 449. doi: 10.3390/jcs8110449.

[8] Verma, R., Kumar, J., Singh, N.K., Rai, S.K., Saxena, K.K., Xu, J. (2022) Design and Analysis of Biomedical Scaffolds Using TPMS-Based Porous Structures Inspired from Additive Manufacturing. *Coatings*. 12, 839.

[9] Burchard, R., Graw, J.A., Soost, C., Schmitt, J. (2023) Stress shielding effect after total hip arthroplasty varies between combinations of stem design and stiffness – a comparing biomechanical finite element analysis. *Int. Orthop*. 47, pp. 1981-1987.

[10] Savio, D., Bagno, A. (2022) When the Total Hip Replacement Fails: A Review on the Stress-Shielding Effect. *Processes*. 10, 612.

[11] Ricciardi, G., Siracusano, L., Micale, E., et al. (2025) Aseptic Loosening in Total Hip Arthroplasty: Pathophysiology, Biomarkers, and Preventive Treatment Strategies. *Appl. Sci*. 15, 9156.

[12] Karaman D, Ghahramanzadeh Asl H.(2025) Flow analysis comparison of network solid and sheet solid structures for Schwarz Primitive. *Proc Inst Mech Eng H*. 239(7): pp. 676-686.

[13] Garofalo, S., Morano, C., Bruno, L., Pagnotta, L. A (2025) Comprehensive Literature Review for Total Hip Arthroplasty (THA): Part 2 – Material Selection Criteria and Methods. *J. Funct. Biomater*. 16, 184. doi: 10.3390/jfb16050184.

[14] Lin, X., Patil, S., Gao, Y.-G., Qian, A. (2020) The bone extracellular matrix in bone formation and regeneration. *Front. Pharmacol*. 11, 757.

[15] Mansour, A., Mezour, M.A., Badran, Z., Tamimi, F. (2017) Extracellular matrices for bone regeneration: a literature review. *Tissue Eng. Part A*. 23, pp. 1436-1451.

[16] Zhao, D., et al. (2022) Osteocytes regulate bone anabolic response to mechanical loading in male mice via activation of integrin α5. *Bone Res*. 10, 49.

[17] Kim, J.-M., Lin, C., Stavre, Z., Greenblatt, M.B., Shim, J.H. (2020) Osteoblast-osteoclast communication and bone homeostasis. *Cells*. 9, 2073.

[18] Dyadyura, K.O., Sukhodub, L.F. (2017) Magnesium-based matrix composites reinforced with nanoparticles for biomedical applications. *Proceedings of the 2017 IEEE 7th International Conference on Nanomaterials: Applications and Properties*, NAP 2017. 04NB14.

[19] Sukhodub, L., Dyadyura, K. (2018) Design and fabrication of polymer-ceramic nanocomposites materials for bone tissue engineering. *J. Nano- Electron. Phys*. 10, 06003.

[20] Bahraminasab, M. (2020) Challenges on optimization of 3D-printed bone scaffolds. *BioMed Eng. OnLine*. 19, 69.

[21] Maharjan, B., Park, J., Kaliannagounder, V.K., Awasthi, G.P., Joshi, M.K., Park, C.H., Kim, C.S. (2021) Regenerated cellulose nanofiber reinforced chitosan hydrogel scaffolds for bone tissue engineering. *Carbohydr. Polym*. 251, 117023.

[22] Panda, A., Dyadyura, K.O., Dmytryshyn, D.V., Smorodin, A., Prokopovich, I.V. (2024) Decision support system for the design process of apatite biopolymer composite parts. *Management Systems in Production Engineering*, 32(4), pp. 548-554.

[23] Panda, A., Dyadyura, K., Valíček, J., Harničárová, M., Kušnerová, M., Ivakhniuk, T., Hrebenyk, L., Sapronov, O., Sotsenko, V., Vorobiov, P., Levytskyi, V., Buketov, A. (2022) Ecotoxicity Study of New Composite Materials Based on Epoxy Matrix DER-331 Filled with Biocides Used for Industrial Applications. *Polymers,* 14, 3275. https://doi.org/10.3390/polym14163275.

[24] Husain, H., Hazdra, Z., Kudlacek, J., Kuchar, J. (2021) Risk factors for B4C composite utilization in tribological processes. In: *Metal 2021 – 30th Anniversary International Conference on Metallurgy and Materials, Conference Proceedings*. Brno, 26-28 May 2021. Ostrava: Tanger Ltd., pp. 801-806. ISSN 2694-9296. ISBN 978-80-87294-99-4. DOI: 10.37904/metal.2021.4186.

Tatyana Ivakhniuk
Department of Public Health
Sumy State University
59, Petropavlivska Street, 40014 Sumy, Ukraine
e-mail: t.ivakhnjuk@med.sumdu.edu.ua

Liudmyla Hrebenyk
ORCID ID: 0000-0002-1510-0763
Department of Biophysics, Biochemistry,
Pharmacology and Biomolecular Engineering
Medical Institute, Sumy State University
2, Rymskogo-Korsakova St., 40007 Sumy, Ukraine
e-mail: l.hrebenyk@med.sumdu.edu.ua

Andrii Dyadyura
ORCID ID: 0009-0001-7126-7007
Medical Institute
Sumy State University
59, Petropavlivska Street, 40014 Sumy, Ukraine
e-mail: erdonshmark@gmail.com

Tibor Krenicky (corresponding author)
ORCID ID: 0000-0002-0242-2704
Technical University of Kosice
Faculty of Manufacturing Technologies
Bayerova 1, 08001 Presov, Slovakia
e-mail: tibor.krenicky@tuke.sk

Liudmyla Primova
ORCID ID: 0000-0002-3442-5010
Department of Biophysics, Biochemistry,
Pharmacology and Biomolecular Engineering
Medical Institute, Sumy State University
2, Rymskogo-Korsakova St., 40007 Sumy, Ukraine
e-mail: l.primova@med.sumdu.edu.ua

Irina Dyadyura
ORCID ID: 0000-0002-5529-6406
Medical Institute
Sumy State University
59, Petropavlivska Street, 40014 Sumy, Ukraine
e-mail: iren.dyadyuren666@gmail.com